Accepted Manuscript

Title: IMPROVING THE PHOTOACTIVITY OF BISMUTH VANADATE THIN FILM PHOTOANODES THROUGH DOPING AND SURFACE MODIFICATION STRATEGIES

Author: Javier Quiñonero Teresa Lana–Villarreal Roberto Gómez

PII: S0926-3373(16)30330-7
DOI: http://dx.doi.org/doi:10.1016/j.apcatb.2016.04.057
Reference: APCATB 14742

To appear in: *Applied Catalysis B: Environmental*

Received date: 3-2-2016
Revised date: 8-4-2016
Accepted date: 27-4-2016

Please cite this article as: Javier Quiñonero, Teresa LanandashVillarreal, Roberto Gómez, IMPROVING THE PHOTOACTIVITY OF BISMUTH VANADATE THIN FILM PHOTOANODES THROUGH DOPING AND SURFACE MODIFICATION STRATEGIES, Applied Catalysis B, Environmental http://dx.doi.org/10.1016/j.apcatb.2016.04.057

IMPROVING THE PHOTOACTIVITY OF BISMUTH VANADATE THIN FILM PHOTOANODES THROUGH DOPING AND SURFACE MODIFICATION STRATEGIES

Javier Quiñonero, Teresa Lana–Villarreal*, Roberto Gómez*

Departament de Química Física i Institut Universitari d'Electroquímica, Universitat d'Alacant, Apartat 99, E-03080 Alicante, Spain

*Corresponding authors : Tel: +34 96 590 3855; email address: teresa.lana@ua.es

Tel: +34 96 590 3748; email address: roberto.gomez@ua.es

Graphical abstract

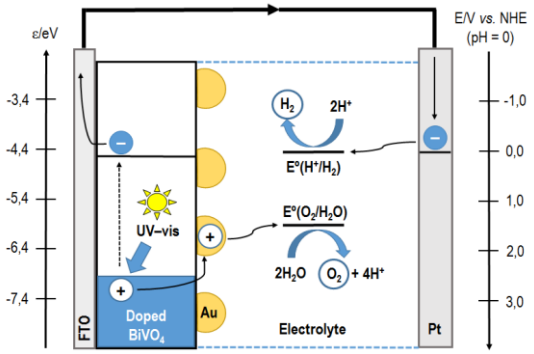

HIGHLIGHTS

- La and Ce doping greatly improves the photoresponse of $BiVO_4$ photoanodes for PEC water oxidation.
- Ce and La doping triggers a significantly shift of the flat band potential to more negative values.
- Surface modification of the pristine and doped $BiVO_4$ photoanodes with Au nanoparticles further enhances the photocurrent.
- Gold nanoparticles act solely as co-catalytic centers without a contribution from visible sensitization.

ABSTRACT

Currently, one of the most attractive and desirable ways to solve the energy challenge is harvesting energy directly from the sunlight through the so–called artificial photosynthesis. Among the ternary oxides based on earth–abundant metals, bismuth vanadate has recently emerged as a promising photoanode. Herein, $BiVO_4$ thin film photoanodes have been successfully synthesized by a modified metal–organic precursor decomposition method, followed by an annealing treatment. In an attempt to improve the photocatalytic properties of this semiconductor material for photoelectrochemical water oxidation, the electrodes have been modified (i) by doping with La and Ce (by modifying the composition of the $BiVO_4$ precursor solution with the desired concentration of the doping element), and (ii) by surface modification with Au nanoparticles potentiostatically electrodeposited. La and Ce doping at concentrations of 1 and 2 at% in the $BiVO_4$ precursor solution, respectively, enhance significantly the photoelectrocatalytic performance of $BiVO_4$ without introducing important changes in either the material structure or the electrode morphology, according to XRD and SEM characterization. In addition, surface modification of the electrodes with Au nanoparticles further enhances the photocurrent as such metallic nanoparticles act as co–catalysts, promoting charge transfer at the semiconductor/solution interface. The combination of these two complementary ways of modifying the electrodes has resulted in a significant increase in the photoresponse, facilitating their potential application in artificial photosynthesis devices.

KEYWORDS: Photoelectroechemistry, water splitting, La doping, Ce doping, gold nanoparticles.

1. INTRODUCTION.

The world is facing serious challenges due to the limited supply of energy and to the global climate change caused by burning fossil fuels. It is widely known that the outstanding technical development experienced by humanity through the employment of non–renewable energy sources has induced an undeniable negative impact on the natural environment. In fact, the use of traditional fossil fuels causes the generation of gases (CO_2, CH_4, SO_2, NO_x…) likely to aggravate certain pollution problems, such as the greenhouse effect and the acid rain. This situation could worsen during the next decades by the sharply growing global energy demand: it has been estimated that global energy consumption will reach almost 27 TW by 2050, while nowadays it is close to 15 TW. The combination of these two factors has motivated the search for new energy sources to minimize the emissions of such pollutant gases and/or economical methods for their recycling (mainly in the case of CO_2) [1].

In this context, artificial photosynthesis –the capture, conversion and storage of solar energy in chemical bonds– stands as a central research subject in the field of renewable energy because it is a very attractive approach to solve the current energy challenges. This is due to its great potential to convert photon energy from sunlight into chemical energy with a minimal environmental impact, as in the case of natural photosynthesis [2]. In fact, nowadays one of the most promising technologies for the production of hydrogen from renewable energy sources is photoelectrochemical (PEC) solar water splitting on semiconductor electrodes because it is a sustainable, carbon neutral and cost–effective process to produce solar fuels [3–5]. The concept of water splitting concept into oxygen and hydrogen was first demonstrated by Fujishima and Honda in 1972 using a TiO_2 photoanode under ultraviolet light irradiation and a dark platinum cathode [6]. Due to the slow kinetics associated with multi–electron and multi–proton transfers (PEC water splitting has approximately three orders of magnitude lower rate than the hydrogen evolution reaction in conventional water electrolysis [7]), water oxidation is particularly demanding and requires high overpotentials. Therefore, many efforts have been made to develop efficient and practical photoanode systems that can oxidize water to O_2 in a stable manner as this is a critical point for the successful construction of high performance and commercially viable PEC cells [3–5].

For enhanced water splitting, an ideal photoelectrode should have a narrow bandgap, high quantum efficiency in the range of visible light, good photochemical stability and photocatalytic activity, and it should be made from earth–abundant elements [3–5]. This is why some inexpensive semiconductor metal oxides have been the primary choice of photoelectrodes for PEC water oxidation during the past few decades. In particular, attention has been focused on TiO_2 (E_g = 3.2 eV, for anatase phase) [8,9], Fe_2O_3 (E_g = 2.2 eV) [10–12] and WO_3 (E_g = 2.7 eV) [13,14] as to utilize at least part of the solar spectrum. However, it seems that none of these binary oxides fulfill all the requirements needed for achieving efficient devices for artificial photosynthesis. Therefore, in the last years, several ternary semiconductor photoelectrodes capable of oxidizing water, generating molecular oxygen, have also attracted a great deal of interest. These include some titanates ($SrTiO_3$ [15,16], $PbTiO_3$ [17], and $BaTiO_3$ [18]) and tantalates ($KTaO_3$ [19,20], $LiTaO_3$ [19,20] and $NaTaO_3$ [19,21]) from the perovskite (ABO_3) family, and certain vanadates ($InVO_4$ [22,23], $BiVO_4$ [24–26] and $FeVO_4$ [27,28]) and wolframates (mainly $CuWO_4$ [29]), with general formula ABO_4. Most of them are characterized by their visible light activity, stability in aqueous electrolytes and low cost. However, the actual conversion efficiencies for both binary and ternary semiconductor metal oxides have been shown to be much lower than their theoretical limits, most likely due to fast charge recombination resulting from poor carrier mobility or slow interfacial charge transfer [30].

Among these semiconductor candidate materials for photosynthetic electrodes, bismuth vanadate ($BiVO_4$), which is an *n*–type semiconductor, has been identified as one of the most promising photoanode materials since the publication of the first report on its use as a photocatalyst in 1998 [24]. $BiVO_4$ is a low–toxicity material with a good chemical/photochemical stability composed of relatively inexpensive elements. Its bandgap is of 2.4 eV (for the monoclinic variety); however, a wide range of values has been reported depending on the considered crystalline phase. Its valence band edge is located at approximately 2.4 V (*vs*. RHE), providing sufficient overpotential for the photogenerated holes to oxidize water, while the conduction band edge is located just close to the level of the H_2O/H_2 couple (0.05 V *vs*. RHE). Although its bandgap is slightly wider than desired for a photoelectrode, the very negative conduction band edge potential compensates for this disadvantage, as not many *n*–type semiconductors absorbing visible light have a conduction band edge potential that is as negative as that of $BiVO_4$ [24–26]. In addition, the

effective masses of electrons and holes in $BiVO_4$ are predicted to be much lower than those of other semiconductors (*e.g.* TiO_2 or In_2O_3) [31,32]. All these facts allow this compound to have a theoretical solar–to–hydrogen (STH) conversion efficiency close to 9.2%. Nevertheless, the typical STH conversion efficiencies of unmodified $BiVO_4$ photoanodes are disappointingly low (lower than 1%) as they suffer from excessive electron–hole recombination and poor photogenerated carrier transport properties [7]. The slow water oxidation kinetics, due to the high kinetic barrier for water oxidation reaction, is another important limitation for the use of $BiVO_4$ in photoelectrochemistry [26].

Recently, many attempts have been made to address one or more of these issues to further improve the efficiency of $BiVO_4$. These include (i) controlling morphologies (film thickness, particle size/shape and porosity) [33–35], (ii) forming composite structures or heterojunctions [36,37] and especially (iii) doping (or alloying) [7,25,38–44] and (iv) coupling with an oxygen evolution catalyst (OEC) [45–55]. In this way, doping strategies have been employed in an attempt to overcome the relatively slow electron transport in $BiVO_4$. In fact, the incorporation into $BiVO_4$ of donor–type dopants such as Ag [25], Cr [7], W [38,39], Mo [40,41], Si [42], Ti [56], Nb [56], Zn [56], Sn [56] or Pd [57], and certain lanthanide cations such as Eu [58] and Dy [59] has been found to enhance the PEC performance of the semiconductor, strengthening its *n*–type characteristics by supplying additional conduction band free electrons and enhancing electric conductivity. Doping also improves carrier separation by creating a space charge region in the solid part of the semiconductor–electrolyte interface. Nevertheless, the slow charge transfer to solution likely remains the performance bottleneck, mainly for driving complex reactions such as water oxidation [26]. Therefore, $BiVO_4$ still requires a catalyst to attain reasonable rates for the transfer of photogenerated holes to solution. In fact, OECs bring a dramatic improvement in the performance of the photoelectrodes by favoring the separation of electrons and holes and reducing the kinetic barrier for PEC water oxidation. However, only a limited number of electrocatalysts are effective for $BiVO_4$ in PEC water oxidation, including “cobalt phosphate” (Co–Pi) [45], Co_3O_4 [46], RhO_2 [41], IrO_x [47], “nickel borate” (Ni–Bi) [48], “cobalt carbonate” (Co–Bi) [49] and FeOOH [50,51].

The present study shows a facile preparation of efficient $BiVO_4$ thin film electrodes coated on FTO and based on a modified metal–organic precursor decomposition (MOD) method followed by a heat treatment previously described in the literature. In an effort to improve the photocatalytic properties of

$BiVO_4$ in PEC water oxidation, these electrodes were modified in two different but complementary ways: (i) by doping with metallic species (La and Ce) and (ii) by surface modification with Au nanoparticles. Surface modification of semiconductors (especially TiO_2) [52] with Au nanoparticles has received attention because, besides acting as co–catalysts for charge transfer processes, these nanoparticles can also induce photoactivity in the range of visible/near infrared light, ascribed to a surface plasmon photoexcitation phenomenon. In this work, both doped and pristine $BiVO_4$ have been modified with gold nanoparticles in order to improve the photoelectrochemical performance of this material [53,54].

2. EXPERIMENTAL SECTION.

2.1. Preparation of pristine $BiVO_4$ electrodes. $BiVO_4$ films were prepared by layer–by–layer coating over conducting glass substrates through a modified MOD method, followed by a thermal treatment [25]. Prior to $BiVO_4$ deposition, fluorine–doped SnO_2 (F:SnO_2, FTO)–coated glass substrates (size: 1 x 2.5 cm^2) were cleaned by sonication (Selecta Ultrasonics) in acetone (Panreac, P. A.) and ethanol (VWR Prolabo Chemicals, 96%) for 15 minutes each, and air dried. Solutions of 0.2 M $Bi(NO_3)_3 \cdot 5H_2O$ (Sigma Aldrich, 98%) in acetic acid (Scharlau, 99%) and 0.03 M $VO(C_5H_7O_2)_2$ (Fluka, 97%) in acetylacetone (Aldrich, 99%), as Bi and V precursors respectively, were mixed, with the help of magnetic stirring, maintaining a Bi:V molar ratio of 1:1. Then, 40 µL of the solution was spread on a clean FTO substrate and spin–coated (Chemat Technology, KW–4A) at a spin rate of 1500 rpm for 10 s. After drying in air, the coated $BiVO_4$ electrodes were annealed at 500ºC for 30 min. The annealing process was performed in air using a programmable furnace (Conatec, 7800), with a heating rate of 5ºC·min^{-1}. This procedure was repeated six times as to determine the optimized film thickness (see Fig. S1).

2.2. Preparation of doped $BiVO_4$ electrodes. The doped $BiVO_4$ films were deposited and annealed following the method described above, but modifying the composition of the precursor solution with the desired concentration (in at% with respect to either Bi or V content) of the doping element (here, La and Ce). Concretely, $La(NO_3)_3 \cdot 6H_2O$ (Fluka, 99%) and $Ce(NO_3)_3 \cdot 6H_2O$ (Strem Chemicals, 99%) were used as La and Ce precursors, respectively.

2.3. Surface modification of pristine and doped $BiVO_4$ electrodes with gold nanoparticles. Au nanoparticles were deposited on the surface of pristine and doped $BiVO_4$ electrodes by a potentiostatic

electrodeposition method at –0.5 V (*vs*. Ag/AgCl) [60]. This was performed for 30 s in a 0.5 M H_2SO_4 (Panreac, 95–98%) aqueous solution containing 2 mM $NaAuCl_4$ (Alfa Aesar, 99%) and 0.125 mM L–cysteine (Aldrich, 97%), which increased the number of electrodeposited Au nanoparticles and controlled their size.

2.4. Photoelectrochemical measurements and electrode characterization. The PEC measurements were conducted in a home–built Pyrex glass cell with a fused silica window and a computer–controlled potentiostat–galvanostat (Autolab, PGSTAT30). A Pt wire and an Ag/AgCl/KCl (3 M) electrode were used as the counter and reference electrodes, respectively. An N_2–purged 0.5 M Na_2SO_4 (Merck, 99%) aqueous solution (pH = 5.44) was used as a working electrolyte for the electrochemical measurements because the stability of the $BiVO_4$ films in Na_2SO_4 (aqueous solution) was good compared to that in other solutions. Photoelectrochemical measurements were also performed using a KH_2PO_4/NaOH buffer solution at pH = 5.80.

The light source was a Xe(Hg) ozone–free lamp (1000 W, Newport Instruments, 66921) equipped with a water filter to minimize the infrared contribution of the beam, and all the PEC measurements were carried out by irradiating the prepared electrodes through the electrode/electrolyte interface (EE illumination). The photon flux intensity was measured by a photodiode power meter (Thorlabs, PM100D), and the typical value was approximately 0.9 $W \cdot cm^{-2}$. For the measurements of incident photon to current conversion efficiency (IPCE) at each wavelength, an ozone–free 300 W Xe arc lamp (Thermo Oriel) was used as a light source, and the wavelength was selected with a monochromator (Oriel Instruments 74100).

The crystalline phase of the prepared $BiVO_4$ films was determined by XRD analysis. A Bruker, D8–Advance X–ray diffractometer operating at room temperature with Cu–Kα radiation (λ=1.5416 Å) at 40 kV and 40 mA was used. The angular velocity was $0.5^{\circ} \cdot min^{-1}$ within a 2θ range between 15º and 70º. A SEM study was carried out to characterize the surface morphology and thickness of the films using a JEOL JEM–1400 field emission scanning electron microscope (FESEM). XPS experiments were done with a VG–Microtech Multilab 3000 spectrometer equipped with a monochromatic Al–Kα source (1486.6 eV), operating at 15 kV and 10 mA. The optical properties of the films were studied by solid–state UV–Vis spectroscopy, using a Shimadzu, UV–2401 PC spectrophotometer equipped with an integrating sphere.

The UV–visible spectral data for the annealed films coated on transparent FTO conducting substrates were recorded in the absorbance mode.

3. RESULTS AND DISCUSSION.

3.1. Pristine $BiVO_4$ films. Fig. 1a shows the XRD patterns for an FTO conductive glass piece prior to and after the deposition of a $BiVO_4$ thin film. Apart from FTO, $BiVO_4$ was the only crystalline phase detected in the thin film. The XRD analysis confirms that the synthesized $BiVO_4$ films are crystalline and present a scheelite structure with a monoclinic phase, with the following lattice parameters: a = 5.1935 Å, b = 5.898 Å, c = 11.6972 Å, $\alpha = \gamma = 90^{\circ}$ and $\beta = 90.387^{\circ}$. The XRD peaks have been indexed according to the JCPD card number 14–0688. As shown in Fig. 1b, the FESEM image of the sample surface shows the typical morphology of a thin film, described as a compact deposit with low porosity. The cross sectional FESEM micrograph (Fig. 1c) shows that the films have an average thickness of around 1 μm. The adhesion of the $BiVO_4$ layer to the conducting substrate was very good. To elucidate the chemical composition along with valence states of the elements present in the films, XPS valence band spectra were recorded. From Fig. 1d, the Bi 4*f* spectrum of $BiVO_4$ consists of two strong symmetrical peaks at binding energies (E_b) 158.9 and 164.2 eV, corresponding to the Bi $4f_{7/2}$ and Bi $4f_{5/2}$ signals, respectively, and which are characteristic of Bi^{3+} species [61]. The V 2*p* XPS spectrum (Fig. 1e) exhibits two peaks at binding energies of 516.5 and 524.0 eV, corresponding to the V $2p_{3/2}$ and V $2p_{1/2}$ peaks. This characteristic spin–orbit splitting confirms the presence of V^{5+} in the sample [61].

The pristine $BiVO_4$ films spin–coated on FTO glass substrates were investigated for the water photooxidation reaction using aqueous 0.5 M Na_2SO_4 (pH = 5.44) as a working electrolyte. First, the electrochemical characterization was done in the dark. As observed in Fig. 2a, the electrochemical response exhibits the existence of small capacitive currents over a wide potential range.

The linear scan voltammogram in Fig. 2b recorded under transient illumination is characterized by the existence of very small dark currents (in agreement with the cyclic voltammogram shown in Fig. 2a) together with anodic photocurrents. These results are thus indicative of water oxidation by the photo–generated holes in the valence band of the $BiVO_4$ thin film electrodes, with the corresponding collection of photo–excited electrons at the conducting substrate. The photocurrent, whose magnitude increases with the applied potential in positive direction, indicates an *n*–type character for the prepared semiconductor

film, and it is remarkably stable. The onset potential is located below 0.0 V (*vs*. Ag/AgCl), which is in agreement with several values found in the literature [23–25]. Interestingly, the shape of the transients shows clear signs of hole trapping at the electrode surface with the appearance of anodic spikes upon illumination. This behavior is due to electron–hole recombination. Although initially the separation of the photogenerated charges takes place, holes are trapped at the electrode surface, thus favoring recombination. In fact, hole trapping at the surface is one of the factors limiting the performance of this electrode material.

The *n*–type character of the as–prepared $BiVO_4$ electrodes was confirmed by constructing Mott–Schottky plots (Fig. S2) in the dark and under illumination. In fact, the $1/C^2$ *vs*. E plot shows the expected linear tendency although only in a limited range of potentials. From the corresponding intercept with the abscissa axis, values of -0.46 V and -0.24 V (*vs*. Ag/AgCl) can be roughly estimated for the flat band potential in the dark and under illumination, respectively. It is worth noting that the flat band potentials value apparently shifts to more positive potentials. This is a clear indication that photogenerated holes are accumulated at the electrode surface shifting downward the conduction band edge. Moreover, and as expected, the charge–carrier density increases under illumination. The flat–band potential of $BiVO_4$ photoanodes has been widely measured in the dark by Mott–Schottky analysis [25,38,41,62–65]. The values reported for comparable pHs are frequently in the range from -0.60 V to -0.50 V (*vs*. Ag/AgCl) and therefore they are slighty more negative that the value obtained here.

In order to confirm that possible local changes of pH at the surface of the photoelectrode during the experiments did not alter the voltammetric results, control experiments were done in a KH_2PO_4/NaOH buffer solution (pH = 5.80). A behavior analogous to that shown in Fig. 2b was observed (see Fig. S3).

3.2. La– and Ce–doped $BiVO_4$ films. Fig. 3a shows the XRD patterns for La (1 at%) and Ce (2 at%) doped $BiVO_4$ thin films, and for a piece of FTO conductive glass. These concentrations led to the best PEC results (see Figs. S4 and S5). Upon lanthanum and cerium doping, there are no significant changes in the XRD patterns compared with those obtained for pristine $BiVO_4$ thin films. No peaks corresponding to other phases are detected. These observations indicate that the monoclinic phase is maintained after the incorporation of either La or Ce in the $BiVO_4$ crystal lattice. This result is consistent with the (i) very small

difference in the ionic radii (in eight fold coordination) for La^{3+} (116 pm), Ce^{3+} (114 pm), and Bi^{3+} (117 pm) and (ii) the fact that the amounts of lanthanum (1 at%) and cerium (2 at%) added to the $BiVO_4$ precursor solution are small. Representative FESEM images of La– and Ce–doped $BiVO_4$ films are shown in Figs. 3b and 3c, respectively. From them, it can be deduced that doping does not induce any significant alteration in the topographical and morphological characteristics of the synthesized thin films. The dopants were also studied by XPS. In the La 3*d* spectrum (Fig. 3d) of the corresponding doping films, the presence of a peak at a binding energy of 834.3 eV, which corresponds to the La $3d_{5/2}$ signal, indicates the existence of La^{3+} species in the studied samples [66]. The Ce 3*d* XPS spectrum (Fig. 3e), obtained for the Ce doped electrodes, is more complex. Mainly, four different peaks organized into two distinct doublets can be identified: one corresponds to the Ce $3d_{5/2}$ signal, formed by two peaks with E_b equal to 882.1 and 887.2 eV, while the other doublet is associated with the signal Ce $3d_{3/2}$, with peaks at 898.1 and 903.4 eV. The lower energy signals in both doublets (those appearing at 882.1 and 898.1 eV) indicate the presence of Ce^{4+} species, while the higher energy signals (887.2 and 903.4 eV) can be related to the existence of Ce^{3+} species in the outer region of the thin film electrodes [67]. These XPS analysis also allow us to determine the atomic percentage of dopant element existing in the samples, which is 0.20 at% for La and 0.37 at% for Ce. They are lower than those in the precursor solutions (1 and 2 at%, respectively). This apparent discrepancy can be attributed to the inhomogeneous distribution of dopant atoms through the $BiVO_4$ structure. Such a difference is often observed in metal–doped semiconductors [68].

To study the doping effects on the PEC water oxidation process, cyclic voltammograms in the dark and linear scan voltammograms under transient illumination for the La (1 at%)– and Ce (2 at%)–doped $BiVO_4$ electrodes were recorded. Doping with La and Ce does not induce major changes in the voltammetric response of the $BiVO_4$ electrodes in the dark (Fig. 4a and 4b). Only a slight increase in the capacitance and in the electrocatalytic activity toward the generation of oxygen is observed. More importantly enhancements of the photocurrent by factors of 2.3 and 4.0 after La and Ce doping, respectively, can be deduced (Fig. 4c and 4d). The photocurrent onset of the La– and Ce–doped $BiVO_4$ photoanodes is very close to that of the undoped electrodes. In addition, there is no saturation in the photocurrents observed for La– and Ce–doped $BiVO_4$ photoanodes in the potential range between 0.0 and

1.0 V (*vs*. Ag/AgCl), indicating the existence of significant recombination for low band bending, probably resulting from kinetic limitations in interfacial charge transfer.

Whereas the low electrical conductivity of the pristine $BiVO_4$ could be responsible for its modest performance, the observed enhanced PEC activity of doped $BiVO_4$ can be attributed to the isomorphic substitution of Bi^{3+} by guest La^{3+} and Ce^{3+}/Ce^{4+} ions. These dopants could alter the band structure of the material, giving rise to an enhanced PEC activity. There also exists the possibility that ultrathin films of lanthanum and cerium oxide are formed on the $BiVO_4$ surface passivating surface states linked to recombination. Furthermore, Ce^{3+} species could also be considered as electron donors energetically located in the bandgap of the host semiconductor, not effective for charge recombination. In such a way, the introduction of Ce ions would increase the majority charge carrier concentration, resulting in additional electron conductivity (*n*–type conductivity) of the $BiVO_4$, which is beneficial for improving the PEC performance of the doped semiconductor photoanodes.

To analyze the effect of introducing dopants on both the majority carrier density and the electrode flat band potential, Mott–Schottky plots for La (1 at%)– and Ce (2 at%)–doped $BiVO_4$ electrodes were recorded (Fig. 5). The flat band potential for both La– and Ce–doped $BiVO_4$ shifts to more negative potential values with respect to the flat band potential of the undoped $BiVO_4$, which is desirable in the case of photoanodes. This has several implications, being the most relevant for practical purposes that it makes feasible to combine $BiVO_4$ photoanodes with a larger number of photocathodes without the need of applying an external bias to achieve water photoelectrolysis. On the other hand, doping leads to an increased concentration of charge carriers in the dark. For La (1 at%) and Ce (2 at%) doped $BiVO_4$ electrodes, a similar carrier density can be calculated, which basically corresponds to twice the $BiVO_4$ charge carrier density (see Table S1).

3.3. La– and Ce–doped $BiVO_4$ films modified with Au nanoparticles. Fig. 6 displays surface FESEM images for pristine, La (1 at%)–doped and Ce (2 at%)–doped $BiVO_4$ films modified with Au nanoparticles. From these micrographs, it can be deduced that the assayed potentiostatic electrodeposition method induces the appearance Au nanoparticle aggregates, which cover most the of the original $BiVO_4$ surface. A comparison of the SEM image for Au NP-covered surface with that of the unmodified surface (Figs. 1 and 3 and insets in Fig. 6) helps identify the Au NPs, which show an average diameter of *ca*. 40 nm. From

the value of the cathodic charge exchanged during the 30-s potentiostatic deposition of Au nanoparticles on the surface of the $BiVO_4$ electrode (Fig. S7) and assuming a near unity faradaic efficiency, the mass of electrodeposited Au per unit surface area was estimated to be of around 16 $\mu g \cdot cm^{-2}$. The corresponding density of Au NPs would be of $2.5 \cdot 10^{10}$ cm^{-2}.

Fig. 7 shows linear scan voltammograms under transient illumination for the $BiVO_4$/Au, La (1, at%)–$BiVO_4$/Au and Ce (2, at%)–$BiVO_4$/Au electrodes, and the corresponding dark cyclic voltammograms (included as insets). In the latter, although no well–defined voltammetric signals attributable to the oxidation/reduction processes of the Au nanoparticles can be identified, larger currents than those for the unmodified electrodes are observed, probably linked to the presence of Au nanoparticles on the electrode surface. On the other hand, linear voltammograms under transient illumination allow us to identify an increase in the photocurrent associated to water photooxidation. These results indicate that the Au nanoparticles deposited on the semiconductor improve the transfer of holes to solution, reducing the recombination of photoinduced electron hole pairs at the electrode surface. Specifically, for $BiVO_4$/Au and Ce (2, at%)–$BiVO_4$ /Au electrodes, the improvement in photoactivity is observed in the entire range of applied potentials under illumination, while for La (1, at%)–$BiVO_4$/Au electrodes, the beneficial effect of the presence of Au nanoparticles on its surface is only observed when the applied potential is sufficiently positive (above 0.5 V *vs.* Ag/AgCl). Considering the changes in the UV-visible spectra (see Fig.S6), there also exists the possibility that the Au nanoparticles act as photosensitizers.

In order to clarify the role of Au nanoparticles in the improvement of the $BiVO_4$ photoresponse, Fig. 8 shows a comparison between the photoaction and UV–vis absorption spectra for $BiVO_4$/Au, La (1, at%)–$BiVO_4$/Au and Ce (2, at%)–$BiVO_4$/Au electrodes. In all cases, the photocurrent action spectra for the different electrodes are related to the absorption spectra, except for the contribution of the Au nanoparticles to the absorption spectra (absorption peak at around 580–590 nm). This indicates that the plasmonic excitation of the Au nanoparticles does not lead to PEC activity [37]. Thus, the improvement in the PEC performance can be explained by assuming that the Au nanoparticles exclusively act as co–catalyst, enhancing hole transfer from the $BiVO_4$ to the electrolyte and diminishing recombination [54]. The fact that Au plasmonic excitation does not lead to electron injection in $BiVO_4$ is probably related to the high energy location of the conduction band edge.

4. CONCLUSIONS.

In summary, we have shown that $BiVO_4$ thin film electrodes prepared by layer–by–layer coating over conducting glass substrates by a modified metal–organic precursor decomposition (MOD) method, followed by a heat treatment, behave as efficient photoanodes for water oxidation. Cyclic and linear scan voltammograms in the dark and under illumination, respectively, have been recorded to obtain insights into the photoactivity of the as–fabricated thin films. This electrode material has displayed a remarkable photoresponse, and two different strategies have been employed to enhance its performance. First, doping $BiVO_4$ with La (1 at%) and Ce (2 at%) increases the photocurrent associated to water photooxidation (by factors of 2.3 and 4.0, respectively). This enhancement has been attributed to the fact that La (III) and Ce (III) modify the band structure of $BiVO_4$ and probably contribute to the passivation of deleterious surface states. In addition, Ce^{3+} species could be considered as shallow level electron donors located in the bandgap. As demonstrated by means of Mott–Shottky plots, the introduction of these ions increases the majority charge carrier concentration, resulting in enhanced electron conductivity (*n*–type conductivity) of the $BiVO_4$, which is beneficial for improving the PEC performance. It is worth noting that these dopants also trigger a 0.2–V shift of the flat band potential toward more negative values, which could be justified by considering the possibility that surface lanthanum and cerium oxygenated species yield a more negatively charged electrode surface. In addition, both pristine and doped electrodes can be subsequently modified with gold nanoparticles, inducing a further enhancement of the electrode photoactivity in all cases, indicating that charge transfer to the electrolyte is improved. These gold nanoparticles are supposed to both improve charge separation and act as a co–catalyst. The modified electrodes reported in this work have the potential to be combined with different cathodes and photocathodes, paving the way for the design of bias–free water splitting devices.

ACKNOWLEDGEMENTS.

Financial support of the Spanish Ministry of Economy and Competitiveness through projects MAT2012–37676 and MAT2015-71727-R (FONDOS FEDER) is gratefully acknowledged.

REFERENCES.

[1] D.G. Nocera, M.P. Nash, Proc. Natl. Acad. Sci. 103 (2006) 15729–15735.

[2] D.G. Nocera, Acc. Chem. Res. 45 (2012) 767–776.

[3] T. Bak, J. Nowotny, M. Rekas, C. Sorrell, Int. J. Hydrogen Energy. 27 (2002) 991–1022.

[4] A.B. Murphy, P.R.F. Barnes, L.K. Randeniya, I.C. Plumb, I.E. Grey, M.D. Horne, Int. J. Hydrogen Energy. 31 (2006) 1999–2017.

[5] M.G. Walter, E.L. Warren, J.R. McKone, S.W. Boettcher, Q. Mi, E.A. Santori, Chem. Rev. 110 (2010) 6446–6473.

[6] A. Fujishima, K. Honda, Nature. 238 (1972) 37–38.

[7] H.W. Jeong, T.H. Jeon, J.S. Jang, W. Choi, H. Park, J. Phys. Chem. C. 117 (2013) 9104–9112.

[8] F. Han, V.S.R. Kambala, M. Srinivasan, D. Rajarathnam, R. Naidu, Appl. Catal. A. 359 (2009) 25–40.

[9] T. Berger, D. Monllor–Satoca, M. Jankulovska, T. Lana–Villarreal, R. Gómez, ChemPhysChem. 13 (2012) 2824–2875.

[10] K. Sivula, F.L. Formal, M. Grätzel, ChemSusChem. 4 (2011) 432–449.

[11] I. Cesar, K. Sivula, A. Kay, R. Zboril, M. Grätzel, J. Phys. Chem. C. 113 (2009) 772–782.

[12] I. Cesar, A. Kay, J.A.G. Martinez, M. Grätzel, J. Am. Chem. Soc. 128 (2006) 4582–4583.

[13] C. Santato, M. Odziemkowski, M. Ulmann, J. Augustynski, J. Am. Chem. Soc. 123 (2001) 10639–10649.

[14] J.A. Seabold, K.–S. Choi, Chem. Mater. 23 (2011) 1105–1112.

[15] T. Watanabe, A. Fujishima, K. Honda, Bull. Chem. Soc. Jpn. 98 (1976) 2774–2779.

[16] M.S. Wrighton, A.B. Ellis, P.T. Wolczanski, D.L. Morse, H.B. Abrahamson, D.S. Ginley, J. Am. Chem. Soc. 98 (1976) 2774–2779.

[17] H.G. Kim, O.S. Becker, J.S. Jang, S.M. Ji, P.H. Borse, J.S. Lee, J. Solid State Chem. 179 (2006) 1214–1218.

[18] J.H. Kennedy, J.K.W. Frese, J. Electrochem. Soc. 123 (1976) 1683–4686.

[19] H. Kato, J. Phys. Chem. B. 105 (2001) 4285–4292.

[20] H. Kato, A. Kudo, Chem. Phys. Lett. 295 (1998) 487–492.

[21] H. Kato, A. Kudo, Catal. Letters. 58 (1999) 153–155.

[22] J. Ye, Z. Zou, M. Oshikiri, A. Matsushita, Chem. Phys. Lett. 356 (2002) 221–226.

[23] C.S. Enache, D. Lloyd, M.R. Damen, J. Schoonman, R. van de Krol, J. Phys. Chem. C. 113 (2009) 19351–19360.

[24] A. Kudo, K. Ueda, H. Kato, I. Mikami, Catal. Letters. 53 (1998) 229–230.

[25] K. Sayama, A. Nomura, T. Arai, T. Sugita, R. Abe, T. Oi, J. Phys. Chem. B. 3 (2006) 11352–11360.

[26] Y. Park, K.J. McDonald, K.–S. Choi, Chem. Soc. Rev. (2013) 2321–2337.

[27] C.D. Morton, I.J. Slipper, M.J.K. Thomas, B.D. Alexander, J. Photochem. Photobiol. A Chem. 216 (2010) 209–214.

[28] S.K. Biswas, J.O. Baeg, Int. J. Hydrogen Energy. 38 (2013) 14451–14457.

[29] J.E. Yourey, K.J. Pyper, J.B. Kurtz, B.M. Barlett, J. Phys. Chem. C 117 (2013) 8707–8718.

[30] F.E. Osterloh, Chem. Mater. 20 (2008) 35–54.

[31] Z. Zhao, Z. Li, Z. Zou, Phys. Chem. Chem. Phys. 13 (2011) 4746.

[32] A. Walsh, Y. Yan, M. Huda, M. Al–Jassim, S. Wei, Chem. Mater. 21 (2009) 547–551.

[33] W. Luo, Z. Wang, L. Wan, Z. Li, T. Yu, Z. Zou, J. Phys. D. Appl. Phys. 43 (2010) 405402

[34] G. Xi, J. Ye, Chem. Commun. 46 (2010) 1893–1895.

[35] J. Su, L. Guo, N. Bao, C.A. Grimes, Nano Lett. 11 (2011) 1928–1933.

[36] Y.H. Ng, A. Iwase, A. Kudo, R. Amal, J. Phys. Chem. Lett. 1 (2010) 2607–2612.

[37] P. Chatchai, Y. Murakami, S. Kishioka, A.Y. Nosaka, Y. Nosaka, Electrochim. Acta. 54 (2009) 1147–1152.

[38] M. Li, L. Zhao, L. Guo, Int. J. Hydrogen Energy. 35 (2010) 7127–7133.

[39] R. Saito, Y. Miseki, K. Sayama, Chem. Commun. 48 (2012) 3833–3835.

[40] W. Yao, H. Iwai, J. Ye, Dalton Trans. (2008) 1426–1430.

[41] W. Luo, Z. Yang, Z. Li, J. Zhang, J. Liu, Z. Zhao, Z. Wang, S. Yan, T. Yu, Z. Zou, Energy Environ. Sci. 4 (2011) 4046–4051.

[42] X. Zhang, X. Quan, S. Chen, Y. Zhang, J. Hazard. Mater. 177 (2010) 914–917.

[43] H. Ye, J. Lee, J.S. Jang, A.J. Bard, J. Phys. Chem. C. 114 (2010) 13322–13328.

[44] G. Lei, Mater. Lett. 62 (2008) 926–928.

[45] T.H. Jeon, W. Choi, H. Park, Phys. Chem. Chem. Phys. 13 (2011) 21392–21401.

[46] M. Long, W. Cai, H. Kisch, J. Phys. Chem C 112(2008) 548–554.

[47] H. Ye, H.S. Park, A.J. Bard, J. Phys. Chem. C. 115 (2011) 12464–12470.

[48] S.K. Choi, W. Choi, H. Park, Phys. Chem. Chem. Phys. 15 (2013) 6499–507.

[49] C. Ding, J. Shi, D. Wang, Z. Wang, N. Wang, G. Liu, Phys. Chem. Chem. Phys. 15 (2013) 4589–4595.

[50] K.J. McDonald, K.–S. Choi, Energy Environ. Sci. 5 (2012) 8553–8557.

[51] J.A. Seabold, K.S. Choi, J. Am. Chem. Soc. 134 (2012) 2186–2192.

[52] T. Lana–Villarreal, R. Gómez, Electrochem. Commun. 7 (2005) 1218–1224.

[53] M. Long, Nano Lett. 3 (2011) 171–177.

[54] C.N. Van, W.S. Chang, J.–W. Chen, K.–A. Tsai, W.–Y. Tzeng, Y.–C. Lin, H.–H. Kuo, H.–J. Liu, K.–D. Chang, W.–C. Chou, C.–L. Wu, Y.–C. Chen, C.–W. Luo, Y.–J. Hsu, Y.–H. Chu, Nano Energy. 15 (2015) 625–633.

[55] N. Sakai, Y. Fujiwara, Y. Takahashi, T. Tatsuma, ChemSusChem. 10 (2009) 766–769.

[56] H. Ye, J. Lee, J.S. Jang, A.J. Bard, J. Phys. Chem. C. 114 (2010) 13322–13328.

[57] G. Lei, Mater. Lett. 62 (2008) 926–928.

[58] A. Zhang, J. Zhang, J. Hazard. Mater. 173 (2010) 265–272.

[59] Q. Wang, H. Liu, J. Li, J. Yuan, W. Shangguan, Catal. Lett. 131 (2009) 160–163.

[60] N. Sakai, Y. Fujiwara, Y. Takahashi, T. Tatsuma, ChemPhysChem. 10 (2009) 766–769.

[61] J. Zhang, B. Wang, C. Li, H. Cui, J. Zhai, Q. Li, J. Environ. Sci. 26 (2014) 1936–1942.

[62] S.J. Hong, S. Lee, J.S. Jang, J.S. Lee, Energy Environ. Sci. 4 (2011) 1781–1787.

[63] K.P.S. Parmar, H.J. Kang, A. Bist, P. Dua, J.S. Jang, J.S. Lee, ChemSusChem. 5 (2012) 1926–1934.

[64] A.J.E. Rettie, H.C. Lee, L.G. Marshall, J. Lin, C. Capan, J. Lindemuth, J.S. McCloy, J. Zhou, A.J. Bard, B. Mullins, J. Am. Chem. Soc. 135 (2013), 11389–11396.

[65] S.J.A. Moniz, J. Zhu, J. Tang, Adv. Energy Mater. 4 (2014) 1–8.

[66] M. Wang, Y. Che, C. Niu, M. Dang, D. Dong, J. Rare Earths. 31 (2013) 878–884.

[67] M.C. Neves, M. Lehocky, R. Soares, L. Lapcik, T. Trindade, Dye. Pigment. 59 (2003) 181–184.

[68] G. Longo, F. Fresno, S. Gross, U.L. Štangar, Environ. Sci. Pollut. Res. (2014) 1–9.

FIGURE CAPTIONS

Fig. 1. (a) XRD patterns for the spin–coated pristine $BiVO_4$ films on FTO, and for the bare FTO substrate. FESEM images for the spin–coated pristine $BiVO_4$ film on FTO (b) top view and (c) cross section. (d) Bi 4*f* and (e) V 2*p* XPS spectra for the $BiVO_4$ film.

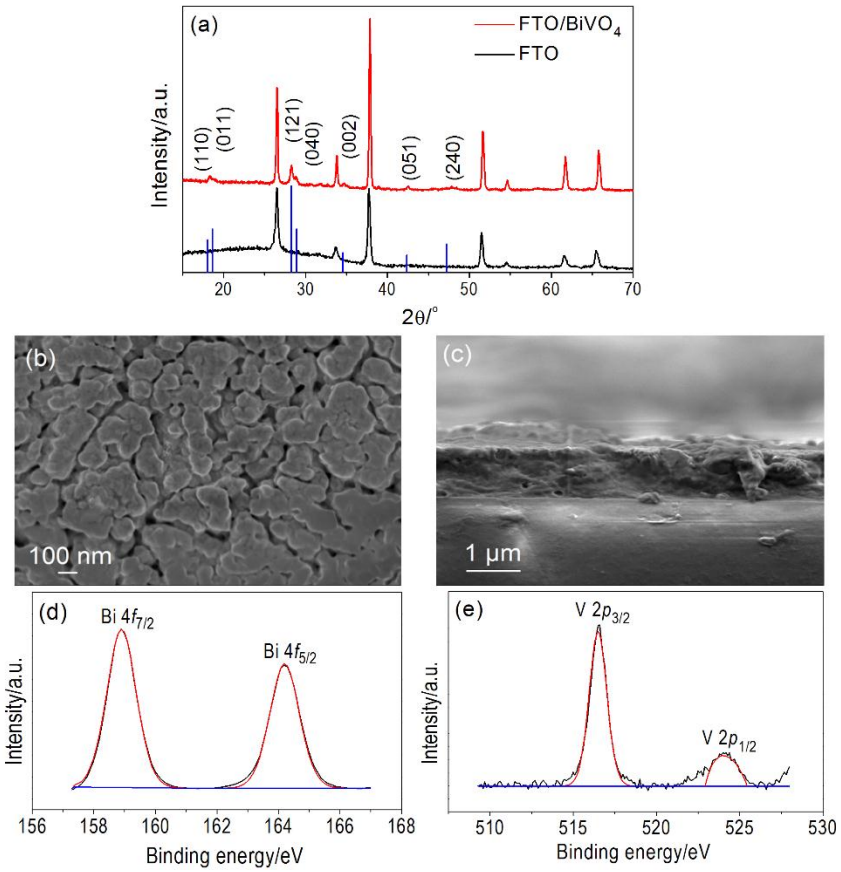

Fig. 2. (a) Cyclic voltammogram (scan rate: 50 mV·s^{-1}) in the dark and (b) linear scan voltammogram (scan rate: 5 mV·s^{-1}) under transient electrolyte–electrode illumination (0.9 W·cm^{-2}, approx.) for pristine $BiVO_4$ thin film electrodes in N_2–purged 0.5 M Na_2SO_4 aqueous solution.

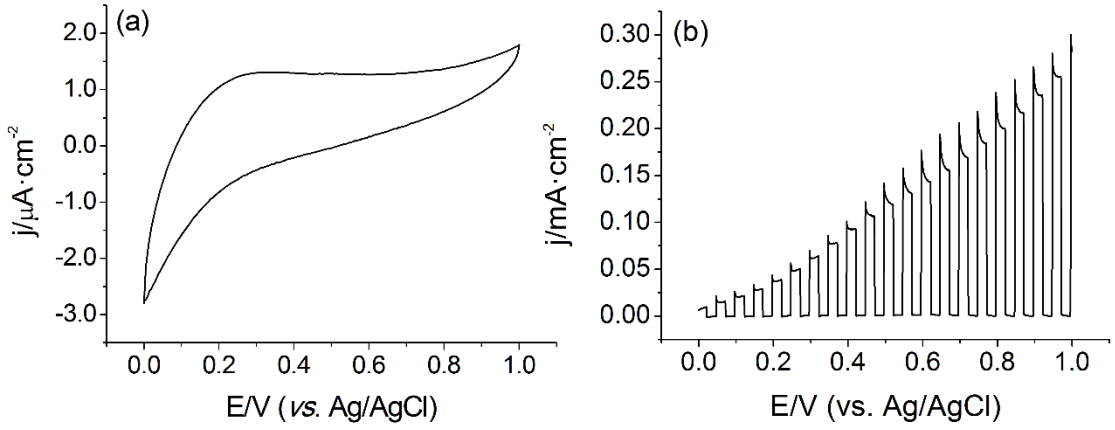

Fig. 3. (a) XRD patterns for the La (1 at%)–doped and Ce (2 at%)–doped spin–coated $BiVO_4$ films on FTO, and for the bare FTO substrate. FESEM images for (b) La (1 at%)–doped and (c) Ce (2 at%)–doped spin–coated $BiVO_4$ films on FTO. La 3*d* (d) and Ce 3*d* (e) XPS spectra of the doped $BiVO_4$ thin films.

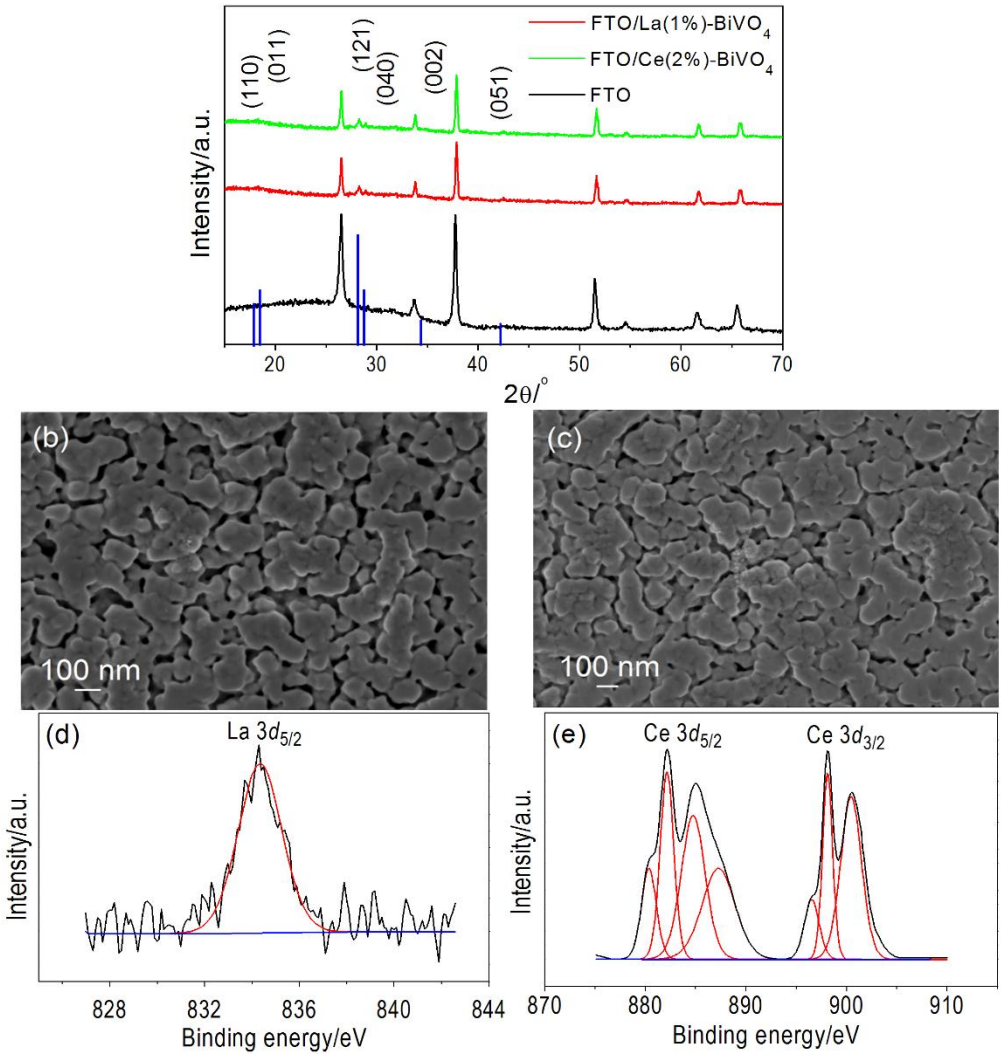

Fig. 4. Cyclic voltammograms (scan rate: 50 mV·s^{-1}) in the dark (a and b) and linear scan voltammograms (scan rate: 5 mV·s^{-1}) under transient electrolyte–electrode illumination (0.9 W·cm^{-2}, approx.) (c and d) for La (1%)– and Ce (2%)–doped $BiVO_4$ films supported on FTO substrates, respectively, in N_2–purged 0.5 M Na_2SO_4 aqueous solution.

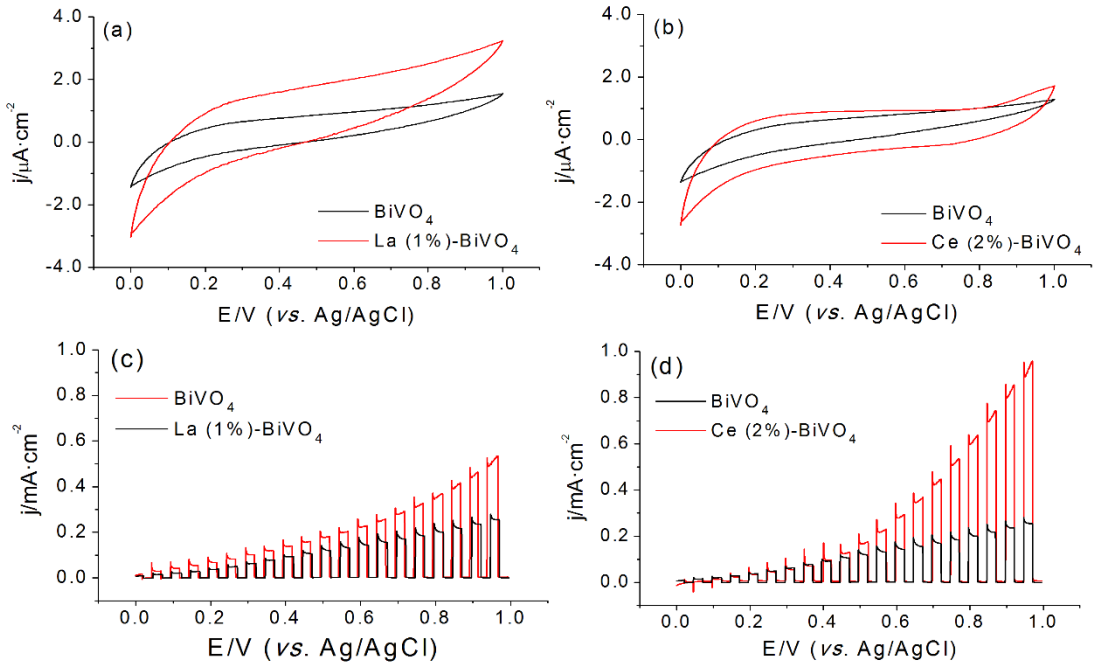

Fig. 5. Mott–Schottky plots (frecuency value: 1 kHz) for La (1 at%)–doped, Ce (2 at%)–doped and pristine $BiVO_4$ electrodes obtained in the dark in N_2–purged 0.5 M Na_2SO_4 aqueous solution.

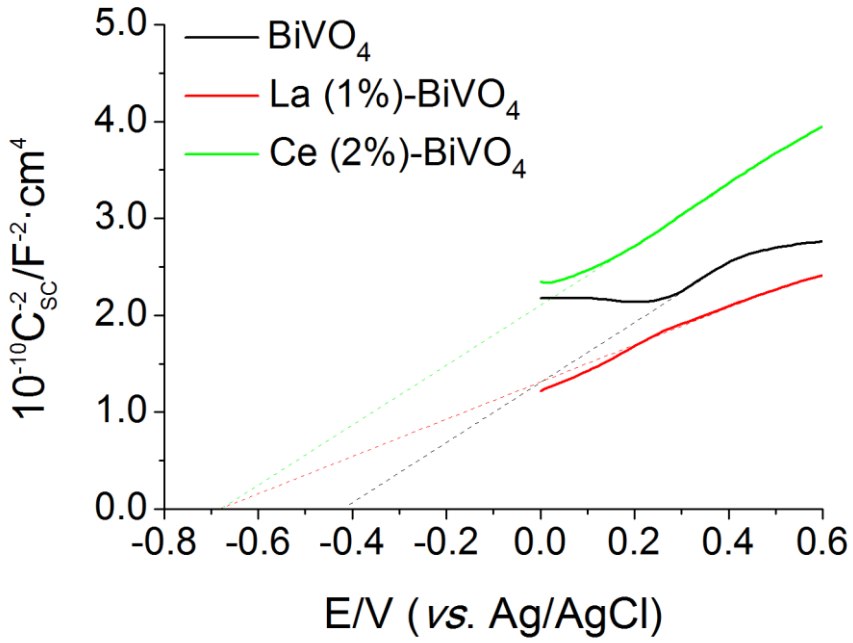

Fig. 6. FESEM images corresponding to top views of (a) $BiVO_4$, (b) La (1 at%)–doped and (c) Ce (2 at%)–doped $BiVO_4$ films modified with Au nanoparticles (portions of Figs. 1(b) and 3(b) and (c) are included as insets).

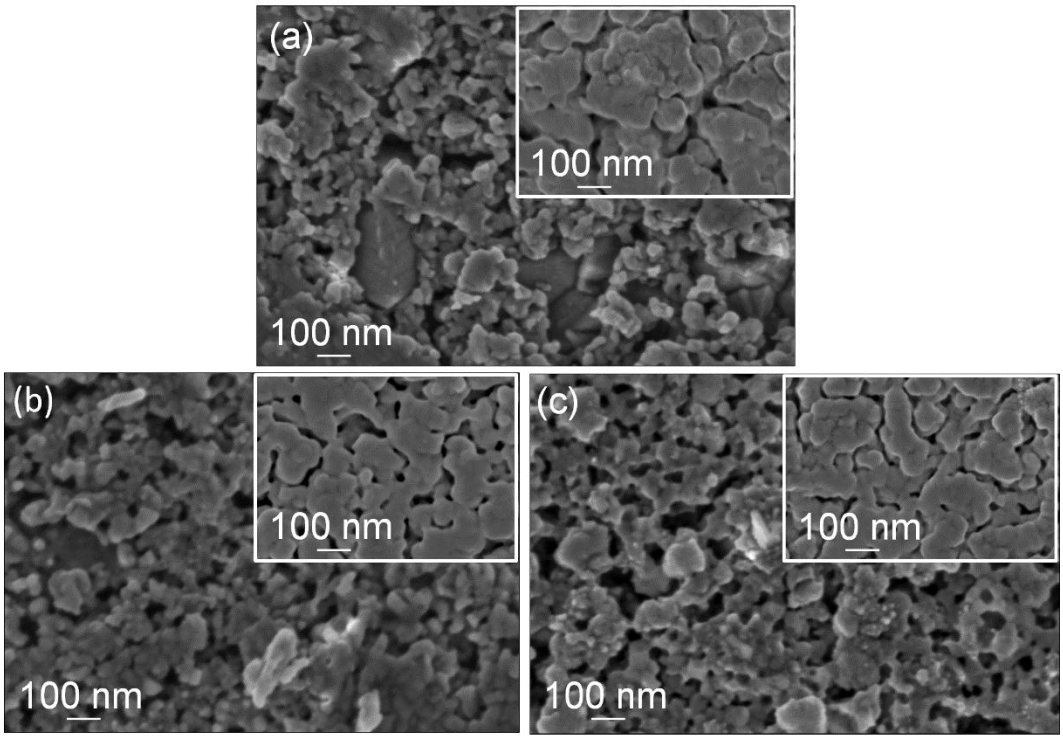

Fig. 7. Cyclic voltammograms (scan rate: 50 mV·s^{-1}) in the dark and linear scan voltammogram (scan rate: 5 mV·s^{-1}) under transient electrolyte–electrode illumination (0.9 W·cm^{-2}, approx.) for (a) $BiVO_4$ and $BiVO_4$/Au, (b) La (1, at%)–$BiVO_4$ and La (1 at%)–$BiVO_4$/Au and (c) Ce (2, at%)–$BiVO_4$ and Ce (2, at%)–$BiVO_4$/Au electrodes in N_2–purged 0.5 M Na_2SO_4 aqueous solution.

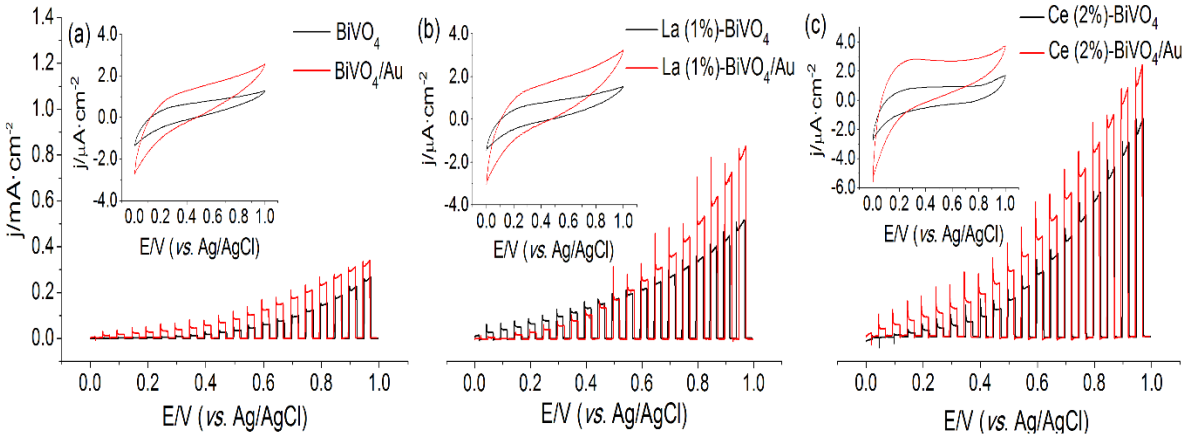

Fig. 8. Correlation between the IPCE (in %) and UV–Vis absorption spectra for (a) $BiVO_4$/Au, (b) La (1, at%)–$BiVO_4$/Au and (c) Ce (2, at%)–$BiVO_4$ /Au electrodes in N_2–purged 0.5 M Na_2SO_4 aqueous solution at 0.9 V (*vs*. Ag/AgCl).